Targeting destabilized DNA G-quadruplexes and aberrant splicing in drug-resistant glioblastoma

Deanna M Tiek[1,5], Roham Razaghi[2], Lu Jin[1], Norah Sadowski[2], Carla Alamillo-Ferrer[3], J Robert Hogg[4], Bassem R Haddad[1], David H Drewry[3], Carrow I Wells[3], Julie E. Pickett[3], William J Zuercher[3], Winston Timp[2], Rebecca B Riggins[1,5]

[1]Department of Oncology, Lombardi Comprehensive Cancer Center, Georgetown University Medical Center, Washington, DC, USA
[2]Department of Biomedical Engineering, Johns Hopkins University, Baltimore, MD, USA
[3]Structural Genomics Consortium, UNC Eshelman School of Pharmacy, University of North Carolina at Chapel Hill, Chapel Hill, NC, USA
[4]Biochemistry and Biophysics Center, National Heart, Lung, and Blood Institute, National Institutes of Health, Bethesda, MD, USA

[5]Correspondence should be addressed to Deanna M Tiek (dmt53@georgetown.edu) and Rebecca B Riggins (rbr7@georgetown.edu) Georgetown University, 3970 Reservoir Road NW, E412 Research Bldg., Washington, DC 20057.

Abstract

Temozolomide (TMZ) is a chemotherapy agent that adds mutagenic adducts to guanine, and is first-line standard of care for the aggressive brain cancer glioblastoma (GBM). Methyl guanine methyl transferase (MGMT) is a DNA repair enzyme that can remove O6-methyl guanine adducts prior to the development of catastrophic mutations, and is associated with TMZ resistance. However, inhibition of MGMT fails to reverse TMZ resistance. Guanines are essential nucleotides in many DNA and RNA secondary structures. In several neurodegenerative diseases (NDs), disruption of these secondary structures is pathogenic. We therefore took a structural view of TMZ resistance, seeking to establish the role of guanine mutations in disrupting critical nucleotide secondary structures. To test whether these have functional impacts on TMZ-resistant GBM, we focused on two specific guanine-rich regions: G-quadruplexes (G4s) and splice sites. Here we report broad sequence- and conformation-based changes in G4s in acquired or intrinsic TMZ resistant vs. sensitive GBM cells, accompanied by nucleolar stress and enrichment of nucleolar RNA:DNA hybrids (r-loops). We further show widespread splice-altering mutations, exon skipping, and deregulation of splicing-regulatory serine/arginine rich (SR) protein phosphorylation in TMZ-resistant GBM cells. The G4-stabilizing ligand TMPyP4 and a novel inhibitor of cdc2-like kinases (CLKs) partially normalize G4 structure and SR protein phosphorylation, respectively, and are preferentially growth-inhibitory in TMZ-resistant cells. Lastly, we report that the G4- and RNA-binding protein EWSR1 forms aberrant cytoplasmic aggregates in response to acute TMZ treatment, and these aggregates are abundant in TMZ resistant cells. Preliminary evidence suggests these cytoplasmic EWSR1 aggregates are also present in GBM clinical samples. This work supports altered nucleotide secondary structure and splicing deregulation as pathogenic features of TMZ-resistant GBM. It further positions cytoplasmic aggregation of EWSR1 as a potential indicator for TMZ resistance, establishes the possibility of successful intervention with splicing modulatory or G4-targeting agents, and provides a new context in which to study aggregating RNA binding proteins.

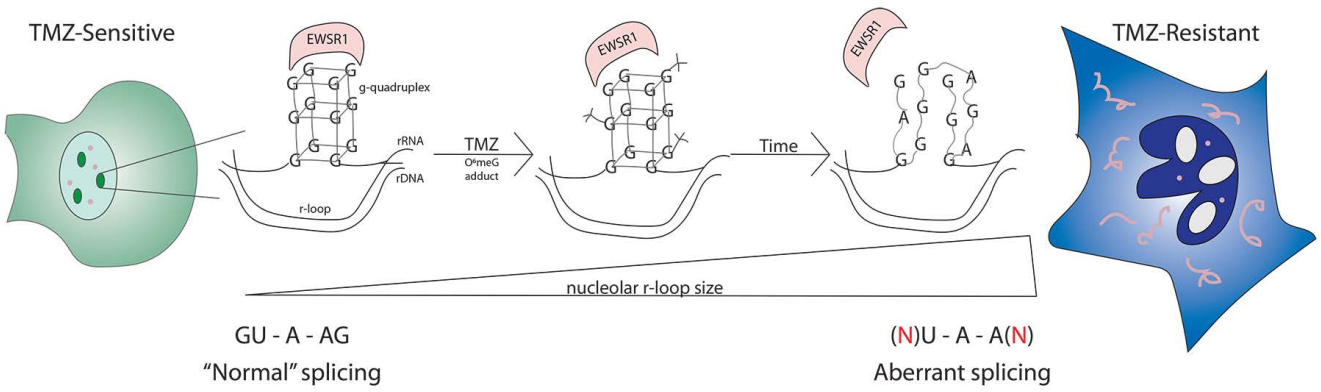

Introduction

Recent epidemiological studies show a decrease in cancer-related mortality rates attributable in part to improved understanding of disease biology and better targeted therapies(Siegel et al., 2019). However, predictive models show mortality rates for the aggressive brain tumor glioblastoma (GBM) will increase in 2019(Siegel et al., 2019). GBM is the most commonly diagnosed glioma and has an abysmal overall survival rate of ~5% at 5 years(Prados et al., 2015; Wen and Kesari, 2008). With a median survival time of ~15 months, it is uniformly fatal(Nizamutdinov et al., 2018). Temozolomide (TMZ; Temodar) is the FDA-approved standard of care first line therapy for GBM in combination with surgery and radiation(Mannas et al., 2014). TMZ causes DNA damage by adding mutagenic adducts to DNA, predominantly O6-methyl guanine, a lesion that can be repaired by the suicide DNA repair protein methyl guanine methyl transferase (MGMT)(Tentori and Graziani, 2009). The overall survival benefit provided by TMZ is ~ 4 months, and rapid development of TMZ resistance occurs at least in part through demethylation of the MGMT promoter, allowing for the expression of MGMT(Zhang et al., 2012). However, efforts to re-sensitize tumors to TMZ by inhibiting MGMT activity have been unsuccessful(Marsoner et al., 2017).

TMZ preferentially targets guanines(Cheung-Ong et al., 2013), critical nucleotides in many DNA and RNA secondary structures(Hänsel-Hertsch et al., 2017). Two structurally and functionally important and distinct G-rich regions are G-quadruplexes (G4s) and splice sites. Previous studies have shown g-quadruplexes (G4s) to be important regulatory elements for oncogenes like *c-MYC*, *KIT*, or *KRAS*(Cogoi and Xodo, 2006; Fernando et al., 2006; Siddiqui-Jain et al., 2002). These G4s have diverse structural and physicochemical properties that suggest a high degree of selectivity, and thus G4s may represent a selective druggable target in multiple cancers(Balasubramanian et al., 2011). In bladder cancer, mutations that disrupt the repressive G4 structure in the *HRAS* promoter lead to increased expression of HRAS, and this can be reversed with a G4-decoy that mimics the wild-type promoter sequence(Membrino et al., 2011).

In contrast, studies of the C9orf72 in amyotrophic lateral sclerosis (ALS) show that expansions of G4 tracts can cause nucleolar stress, deregulate alternative splicing, and alter RNA binding protein localization(Haeusler et al., 2014). Nucleolar stress, manifested as changes in nucleolar size and circularity, is a poor prognostic factor in many cancers, including GBM(Stamatopoulou et al., 2018). Changes in alternative splicing patterns are widespread in GBM, with prior work suggesting that GBM is "addicted to splicing"(Braun et al., 2017). One family with essential functions in RNA processing in cancer and neurodegenerative diseases (NDs) is the FET family of proteins, consisting of FUS, EWSR1, and TAF15(Svetoni et al., 2016). The aggregation-prone properties of the FET proteins have established FUS as a prototype to study protein aggregation, and as a biomarker for ALS and frontotemporal

dementia (FTLD)(Svetoni et al., 2014). EWSR1 has similar aggregation-prone properties(Harrison and Shorter, 2017) but is more commonly studied as a fusion protein with Fli1 in Ewing's sarcoma(Grünewald et al., 2015). FET proteins also are involved in DNA repair(Izhar et al., 2015), can bind the G4 secondary structure of DNA and RNA(Takahama et al., 2011), and play roles in isoform fate(Luo et al., 2015).

Here, we exploit the known mechanism of action of TMZ, which causes a mutagenic O6-methylguanine adduct, to establish the role of guanine mutations in disrupting DNA secondary structures in GBM and to test whether these mutations have functional impacts on TMZ-resistant GBM that can be targeted pharmacologically. We found mutations in the G-rich G4s and splice sites which confer increased responsiveness to a G4 stabilizing drug (TMPyP4) and a novel splicing kinase inhibitor (CLK2i) in TMZ-resistant cells. We also found a differential stress response to DNA damaging agents with increased nucleolar RNA:DNA hybrid R-loops, and nucleolar stress. We further identify mislocalization of the G4- and RNA-binding protein EWSR1, which forms amyloid-like cytoplasmic aggregates in TMZ-resistant cells that are also identified in GBM clinical specimens. This study establishes a link between both altered DNA secondary structure and splicing deregulation in TMZ-resistant GBM, and positions cytoplasmic aggregation of EWSR1 as a potential indicator for TMZ resistance and potential successful intervention with splicing modulatory or G4-targeting agents.

Results

TMZ-induced guanine mutations

Temozolomide (TMZ; Temodar), the FDA-approved standard of care first-line therapy for glioblastoma (GBM), adds mutagenic adducts to guanine, the most prevalent being O6-methylguanine. To determine the role of guanine (G) mutations in TMZ-resistance we performed whole genome sequencing (WGS) on human GBM cell lines that are TMZ-sensitive cells (42MBGA), have acquired resistant to TMZ through an *in vitro* selection against TMZ (42MBGA-TMZres)(Tiek et al., 2018), or that are intrinsically TMZ-resistant (T98G). Acquired and intrinsic TMZ-resistant cells had significantly increased single nucleotide mutations relative to the TMZ-sensitive cells (Fig. 1a). Further analysis showed G>A, and C>T mutations were most enriched in TMZ-resistant cells (Fig. 1b). These results are consistent with the previously defined Signature 11 (increased C>T mutations) that is enriched in GBM patient samples and has a probable association with TMZ treatment(Alexandrov et al., 2013).

Two G-rich regions that are functionally and structurally important in cancer are G-quadruplexes (G4s) and splice sites. G4s can readily be detected by bioinformatic analysis of WGS. To test the hypothesis that G4 structures would be perturbed in TMZ-resistant cells, we used Quadron, an algorithm that integrates sequence information to detect tracts of Gs and Cs with characteristic surrounding sequence features of G4s(Sahakyan et al., 2017). After all G4s were detected, we identified G4 sequences unique to each cell line, and these unique G4s were then used to identify significantly enriched motifs using Multiple Em for Motif Elicitation (MEME)(Bailey and Elkan, 1994). In TMZ-sensitive 42MBGA cells the top three significantly enriched G-rich sequences contain solely G's as hypothesized (Fig. 1c). However, in the acquired resistant 42MBGA-TMZres we found enrichment of a sequence with higher representation of A and T's (Sequence 3, Fig. 1c). The T98G line, which is intrinsically resistant and was not selected in culture with TMZ treatment, showed enrichment of C- and G/A-rich motifs (Fig. 1c). These potential structural changes caused by mutations in G4s in the TMZ-resistant cells were then validated by immunofluorescence (IF) with the G4-detecting monoclonal antibody BG4. Confirming prior studies(Biffi et al., 2013) showing BG4 specifically binds DNA G4s *in vivo*, treatment of 42MBGA cells with DNAse I abrogated specific nuclear BG4 staining (Fig. 1d; Supplementary Fig. 1a). In the TMZ-sensitive 42MGBA cells, discrete nuclear puncta were detected by the BG4 antibody, in addition to more diffuse nucleolar staining (Fig. 1d; white arrows). In the acute TMZ-treated 42MGBA wild type (WT) cells and both TMZ-resistant cell lines, there were no longer discrete G4 nuclear puncta, which corroborated our WGS data (Fig. 1e-g). We then hypothesized that if disruption of G4 sequences played a functional role in TMZ-resistance, a G4-stabilizing drug may be more effective as a second line treatment in TMZ-resistant cells (Fig. 1h). Treatment with TMPyP4, a G4-stabilizing drug, caused a

slight increase in the punctated BG4 staining pattern in 42MBGA-TMZres cells (Supplementary Fig. 1b,c). In the resistant cell lines, TMPyP4 treatment induced a significant G2/M arrest and decreased cell proliferation with increased subG1 fraction in the acquired resistant cell line, with had minimal effects on cell cycle profile and a slight decrease in growth in the TMZ sensitive cell line (Fig. 1 i-k). These data support the hypothesis that G4-disrupting G mutations have a functional, and potentially targetable, role in TMZ-resistant GBM.

Acquired nucleolar changes with TMZ-induced mutations in G-quadruplexes

G4s are abundant in nucleoli, major stress organelles in cells undergoing DNA damage, and nucleoli are also poor prognostic markers in several cancers, including GBM[24,25]. Nucleoli are formed in part by regions of 5 acrocentric chromosomes: 13, 14, 15, 21, and 22. Metaphase spreads were previously performed on 42MBGA vs. 42MBGA-TMZres cell lines which showed an increase in total chromosome number in the 42MBGA-TMZres cell line(Tiek et al., 2017). We reanalyzed these data to determine if the acrocentric, or nucleolar-forming, chromosomes were hyper-enriched in the acquired resistant cell line, and showed the resistant cells had a significantly higher fraction of acrocentric chromosomes compared to their TMZ-sensitive parental line (Fig. 2a). Next, we adapted the iNO score as a method of quantifying nucleolar stress that accounts for both size and roundness of nucleoli(Stamatopoulou et al., 2018). Using IF detection and automated analysis of the nucleolar protein nucleolin (NCL) to determine nucleolar size and circularity (Fig. 2b), we found significant increases in nucleolar size associated with both acute TMZ treatment and intrinsic resistance (Fig. 2c), and significant decreases in circularity, or nucleolar roundness, in acute TMZ treated and both acquired and intrinsic TMZ-resistant nucleoli (Fig. 2d). Within nucleoli, RNA polymerase I (RNAPI) transcribes ribosomal RNAs (rRNA), which can hybridize to antisense ribosomal DNA (rDNA) to form rRNA:rDNA R-loops (Lindström et al., 2018). We then used the R-loop specific antibody S9.6 to visualize nucleolar R-loop changes(König et al., 2017). The TMZ-sensitive 42MGBA cells showed DNA-damage induced punctated R-loop accumulation throughout the nucleus(Gorthi et al., 2018) when treated with TMZ (Fig. 2f), compared to the nucleolar staining in untreated 42MBGA-WT (Fig. 2e). However, TMZ-resistant cell lines showed a robust increase in nucleolar R-loop accumulation, rather than nucleoplasmic puncta associated with a normal DNA damage response(Gorthi et al., 2018) (Fig. 2g-i). We validated the specificity of the R-loop antibody, S9.6, by treating cells with RNAse H, which digests R-loops. This treatment abrogated specific nucleolar staining (Supplementary Fig. 1d). Overall, TMZ-resistant GBM cells exhibit an increase differential nucleolar stress response with an increase in the number of acrocentric chromosomes and nucleolar size, a decrease in nucleolar circularity, and differential R-loop staining patterns.

CLK2 inhibition preferentially targets TMZ-resistant cells

WGS analysis further identified a significant increase in mutations in the G-rich splice sites in TMZ-resistant cells (Fig. 3a). Splicing mutations and altered splicing patterns are characteristic of many cancers, including GBM(Bejar, 2016). To quantify changes in categories of splicing events in the TMZ-resistant vs sensitive cells, we performed nanopore cDNA sequencing to interrogate full length transcripts. Using Full-Length Alternative Isoform analysis of RNA (FLAIR(Tang et al.)) and SUPPA2(Trincado et al., 2018) pipelines, we identified marked enrichment of skipped exons in acquired and intrinsic TMZ-resistant cells (Fig. 3b). Several splicing factor families drive exon inclusion relative to exclusion events, including serine/arginine rich proteins (SRs). SR protein activity and localization are dependent upon their phosphorylation status, which can be altered by DNA damage(Sakashita and Endo, 2010). We also found that the DNA-damaging TMZ treatment induced a significant decrease in the phosphorylation of SR proteins (pSRs) in TMZ-sensitive cells where DNA damage was measured by the presence of the double-strand break marker γH2AX (Fig. 3c). Dephosphorylation of pSRs was not observed in either TMZ-resistant cell line post TMZ-treatment (Fig 3c), suggesting altered pSR function in TMZ-resistant cells. pSRs can bind both introns and exons to determine isoform fate through exon inclusion or exclusion events, where SR proteins that are not hyperphosphorylated are less competent to dictate isoform direction(Shepard and Hertel, 2009). Therefore, we sought to phenocopy the decrease in pSRs caused by TMZ treatment in the sensitive cells by inhibiting a pSR upstream regulator, the cdc2-like kinases (CLKs), in TMZ-resistant cells. CLKs catalyze the nuclear hyperphosphorylation of multiple SR proteins(Agarwal et al., 2011), with public data suggesting an association of higher CLK2 expression with poor overall survival and increased grade in brain cancers (Fig. 3d,e). Our acquired and intrinsic TMZ-resistant GBM cells also showed a robust increase in CLK2 protein expression as compared to the TMZ-sensitive line (Fig. 3f). Treatment of TMZ-resistant cells with a novel and potent CLK inhibitor with increased selectivity for CLK2 (GW807982X, referred to as CLK2i) derived from the Published Kinase Inhibitor Set (PKIS)(Drewry et al., 2014) led to a decrease in SR phosphorylation at 30 minutes (Supplementary Fig. 2a-e(Elkins et al., 2016; Tavares et al., 2004; Wells et al., 2018)), and caused significant G2/M arrest, apoptosis, and decrease in cell growth selectively in TMZ-resistant cells (Fig. 3g-i). Importantly, CLK2i treatment did not cause significant changes to growth rates or cell cycle, and only a modest increase in the apoptotic fraction, in the immortalized non-cancerous brain oligodendrocyte cell line, MO3.13 (Fig. 3g-i). These data support a model in which TMZ-resistant GBM cells have rewired their splicing regulatory machinery over time, as an increase in CLK2 expression was not observed following acute TMZ treatment. Therefore, stably TMZ-resistant cells exhibit deregulation

of SR protein phosphorylation and CLK2 function, and pharmacological inhibition of CLK2 may selectively target these alterations in the context of TMZ resistance.

EWSR1 mislocalization and amyloid-like cytoplasmic aggregation in TMZ-resistant cells and GBM clinical specimens

Considering the collective deregulation of G4s, nucleoli, and splicing identified in TMZ resistant GBM cells, we sought a robust, independent marker that might be an indicator for TMZ resistance and, potentially, CLK2i efficacy in the future. EWSR1 is member of the FET family of proteins, which also includes FUS and TAF15, where FUS is an established biomarker in many central nervous system disorders(Svetoni et al., 2016). EWSR1 can bind DNA G4 structures(Takahama et al., 2011), relocates to nucleoli following UV-induced DNA damage(Paronetto et al., 2011), and plays key functional roles in splicing and DNA damage responses(Paronetto et al., 2011). An endogenous basal stain of EWSR1 showed a dramatic difference in staining between TMZ-sensitive vs. resistant cells. The nuclear staining in TMZ-sensitive cells was in marked contrast to both the nuclear and cytoplasmic amyloid-like aggregates, with a reversed image to better visualize the cytoplasmic staining, seen in acute TMZ-treated and resistant cells (Fig. 4a). However, overall expression of EWSR1 did not increase with TMZ resistance (Fig. 4d). Cytoplasmic EWSR1 aggregates were validated by a second antibody from a different vendor and host species (Supplementary Fig. 3a). We used high resolution stimulated emission depletion (STED) microscopy to better resolve the structure of these aggregates, which showed discrete protein puncta within the cytoplasmic aggregates in both TMZ-resistant cell lines (Fig. 4b,c), and confirmed that the amyloid-like aggregates were specific to the cytoplasm, but not present in the nucleus (Supplementary Fig. 3b-f).

Cytoplasmic aggregation of EWSR1 could suggest a potential role for RNA buffering, a defining feature of mis-localized RNA binding proteins in neurodegenerative diseases(Maharana et al., 2018) where lower RNA concentration in the cytoplasm has been hypothesized to allow the aggregation of these proteins. As EWSR1 has already been shown to relocate to the nucleoli under stressed conditions, we sought to decrease the local RNA concentration and cause a stress response with low dose Actinomycin D (ActD) treatment to test both the new stress response and potential role of RNA in EWSR1 aggregation. Low dose ActD treatment led EWSR1 to accumulate around the nucleoli, which is denoted by R-loops (Fig. 4e). STED imaging of these structures better resolved EWSR1, with 42MBGA cells showing a horseshoe shaped staining pattern that did not link to each other (Fig. 4f). By contrast, EWSR1 formed a linked structure between the droplets in both the acquired and intrinsic TMZ-resistant cells (Fig. 4g,h). This further suggested a role for RNA buffering in EWSR1 aggregation. The

TMZ-resistant cells showed EWSR1 to form protein strands with decreased local RNA concentration in the nucleoli, which should be studied further in the future. In addition, dual staining of EWSR1 and DNA G4s showed colocalization in the TMZ-sensitive cell line that was abrogated with TMZ resistance (Supplementary Fig. 4a-c), further suggesting that the deregulation of G4s identified in TMZ -resistant cells (Fig. 1e-g) can disrupt the localization of G4-binding proteins like EWSR1. However, EWSR1 amyloid-like aggregates do not drive or maintain TMZ-resistance, as knockdown of EWSR1 had minimal effects on cell cycle profile or specific cell death in TMZ-resistant cells (Supplementary Fig. 5a-e). We further used Leptomycin B (LMB), an inhibitor of the nuclear export protein CRM1, to show that EWSR1 was efficiently trafficked to and from the cytoplasm in both TMZ-sensitive and -resistant lines (Supplementary Fig 5f-h). Ectopically expressed, YFP-tagged EWSR1 caused non-endogenous ribbon-like formation of EWSR1 in the cytoplasm in the TMZ-resistant cell lines, preventing further overexpression experiments (Supplementary Fig. 5i,j) and there were no significant changes in EWSR1 or CLK2 isoform profile (Supplementary Fig. 6a-d). Overall these studies suggest that EWSR1 is the first, to our knowledge, amyloid-like aggregating protein in GBM, where RNA buffering and deregulation of G4 structures may play a role in its aggregation.

A key limitation of studies conducted in cell culture is their dependence on *ex vivo* models that have been in culture for decades. To determine whether EWSR1 cytoplasmic aggregates were also present in clinical GBM, we stained a cohort of 15 GBM samples for EWSR1 where 9 of the 15 tumors were positive for EWSR1 cytoplasmic amyloid-like aggregates (Fig. 5a,b). This establishes a clinically relevant framework for future studies to determine the functional role of EWSR1 amyloid-like aggregation in GBM.

Discussion

Since the pivotal 2005 clinical trial which changed GBM standard of care to the Stupp regimen - adjuvant TMZ post-surgery and radiation - TMZ has been almost exclusively used in brain cancers, despite adding only a few months to median overall survival(R et al., 2005). Given the lack of successful FDA-approved second-line treatments for GBM, we sought to identify possible dependent pathways that could be targeted in TMZ-resistant GBM(De Vleeschouwer et al., 2017). However, TMZ is rarely used in other cancers, and the 400+ clinical trials to-date that have attempted to repurpose chemotherapeutic or targeted agents from other cancers have failed to provide benefit in GBM(Vanderbeek et al., 2018). We therefore looked to other central nervous system (CNS) disorders for insight. Mechanistic studies in CNS disorders, including neurodegenerative diseases (NDs), show pathological disruption of DNA and RNA secondary structures(Bernat and Disney, 2015), splicing(Mills and Janitz, 2012), and aberrant localization of RNA binding proteins(Hanson et al., 2012). We therefore reframed our strategy for addressing TMZ-resistance in the context of nucleotide secondary structure, RNA processing and RNA binding proteins in TMZ-resistant GBM.

As the first anticancer drugs were DNA-targeting, and still play a major role in cancer treatments, we proposed to determine downstream effects of guanine-focused DNA damage(Balasubramanian et al., 2011). Guanine is the most readily oxidized base, with the loss of an electron creating a hole that is preferentially targeted by spontaneous DNA damage, an event whose impact is compounded in tracts of guanines (Bacolla et al., 2013; Bravaya et al., 2010). The established mechanism of action of TMZ is the addition of a mutagenic O6-methyl adduct to guanines(Zhang et al., 2012). Guanines are critical nucleotides that stabilize many essential DNA and RNA secondary structures(McRae et al., 2017) and are the target of many other chemotherapeutic agents(Cheung-Ong et al., 2013). It also has previously been shown that TMZ-treated GBM has a characteristic mutational signature of C>T(Alexandrov et al., 2013). By performing whole genome sequencing (WGS), we found both C>T and G>A mutations to be enriched. We focused on two key G-rich regions – G-quadruplexes (G4s) and splice sites – to assess their functional roles in TMZ-resistance. We show sequence- and conformation-based changes in G4s by WGS and immunofluorescence, respectively, in TMZ-sensitive vs. acute TMZ treated and TMZ-resistant GBM cells. We also demonstrate that the G4-targeting ligand TMPyP4 is more growth-inhibitory in TMZ-resistant lines. Previously published studies demonstrate the efficacy of other G4 ligands in multiple cancer cell lines, with CNS-derived models being the most sensitive(Nakamura et al., 2017). Therapeutic targeting of G4s in ALS can also decrease toxic hexanucleotide repeat foci and dinucleotide repeat proteins, leading to less disease phenotypes *in vitro*(Simone et al., 2018). Therefore, this avenue of targeting nucleotide secondary structure changes post-chemotherapy should be

investigated further in the future, but will require the development of interventions that can cross the blood-brain barrier (BBB), as TMPyP4 cannot(Fujiwara et al., 2015).

TMZ-resistant GBM cells show an increase in a second critical DNA:RNA secondary structure: nucleolar R-loops. Nucleoli are major stress organelles whose size and circularity are correlated to cancer grade(Stamatopoulou et al., 2018). The increase in nucleolar R-loops in TMZ-resistant cells is intriguing, as a normal DNA-damage response would result in punctated R-loops throughout the nucleus(Gorthi et al., 2018), which we observe in TMZ-sensitive cells in response to TMZ. However, this pattern is lost in TMZ-resistant cells. In other settings, nucleolar R-loop increases have been shown to induce genome instability(Gan et al., 2011), correlate with rDNA mutations, and an aberrant DNA damage response(Lindström et al., 2018). This further confirms what others have suggested(Cui et al., 2010), that there may be a differential DNA damage response between TMZ-sensitive and -resistant cells.

We further focused on G-rich splice sites and their potential contribution to aberrant regulation of alternative splicing, a hallmark of many cancers(Gonçalves et al., 2017). We showed that splicing mutations are enriched in the TMZ-resistant cell lines. We then performed Oxford Nanopore Technology (ONT) full-length sequencing to more globally assess whether a specific event type was enriched in the TMZ-resistant cells, and this identified marked enrichment of exon skipping events. The CLK family of kinases regulates the nuclear hyperphosphorylation of SR proteins, key regulators of exon fate. We further showed SR proteins to be differentially phosphorylated in TMZ-sensitive versus -resistant cells following TMZ treatment, found an increase in CLK2 expression in TMZ-resistant cells, and demonstrated that a novel CLK2 kinase inhibitor is more growth-inhibitory in TMZ-resistant lines. Targeting splicing broadly is an active area of research with clinical trials underway in *SF3B1* mutant cancers and neurological diseases(Seiler et al., 2018), and our data suggest that these efforts should be expanded to TMZ-resistant GBM.

Our data further identify EWSR1 as the first, to our knowledge, aggregating RNA-binding protein in TMZ-resistant GBM. We show that EWSR1 amyloid-like aggregates form in response to acute TMZ treatment and are abundant in independent models of acquired and intrinsic TMZ resistance. Preliminary evidence also shows that cytoplasmic EWSR1 aggregates also are present in GBM clinical samples. This aggregation phenotype is similar to DNA damaged-induced FUS aggregation observed in FUS-ALS motor neurons(Naumann et al., 2018). RNA buffering may also play a role in the aggregation phenotype, as we show that inhibition of nucleolar rRNA transcription by acute Actinomycin D (ActD) treatment can induce ribbon-like strands of EWSR1 around the nucleolus, though the local concentration of EWSR1 would presumably be increasing as well. The last factor we explored is the ability of DNA secondary structures to alter protein localization. The inability of EWSR1 to bind the mutated G4s in the

TMZ-resistant lines suggest this may affect the normal function and proper regulation of EWSR1 in both splicing and DNA repair. Overall, our data suggests potential overlapping functions of the cytoplasmic aggregates of EWSR1 with other neurodegenerative diseases, and further studies may provide insight on different upstream regulators between DNA damage-induced amyloid-like aggregation in CNS disorders and possibly other chemotherapy-treated cancers. However, significantly more research needs to be conducted to determine what part DNA and RNA secondary structures, RNA processing and RNA binding protein amyloid-like aggregates play in GBM maintenance and TMZ-resistance.

Materials and Methods

Cell Lines and Culturing Conditions

Immortalized human oligodendrocyte MO3.13 cells were a kind gift from Dr. Alexandra Taraboletti (Lombardi Comprehensive Cancer Center, LCCC). Temozolomide (TMZ) sensitive 42MGBA cells were provided by Dr. Jeffrey Toretsky (LCCC), and the *de novo* TMZ resistant T98G cell line was provided by Dr. Todd Waldman (LCCC). The acquired TMZ resistant 42MGBA-TMZres cell line variant was developed by our lab and previously described(Tiek et al., 2018). All cells tested negative for *Mycoplasma* contamination and were maintained in a humidified incubator with 95% air: 5% carbon dioxide. All cell lines were fingerprinted by the LCCC Tissue Culture Shared Resource to verify their authenticity using the standard 9 STR loci and Y-specific amelogenin. The 42MGBA-TMZres cells are documented to be of the same origin as their parental cell line. MO3.13, 42MGBA, 42MGBA-TMZres, and T98G cells were grown in Dulbecco's Modified Eagle Medium (DMEM, high glucose, ThermoFisher, #11965092) with 10% FBS.

Immunofluorescence

Cells were seeded at a density of 25,000-30,000 cells onto 18mm diameter #1.5 round coverslips (VWR, #101413-518) in 12-well dishes (day1). They were allowed to attach to the coverslips for a full day (day2). On the following day (day3), the media was removed, cells were washed 3x with PBS, and then fixed and permeabilized in 3.2% paraformaldehyde (PFA) with 0.2% Triton X-100 in PBS for 5 minutes at room temperature. Three washes were performed with PBS in the 12-well plate, then coverslips were inverted onto 120 µL of primary antibody in the antibody block (0.1% gelatin with 10% normal donkey serum in dH2O) on strips of parafilm and incubated for two hours. Coverslips were first incubated with either BG4 (Sigma MABE1126; 1:150), EWSR1 (Rabbit mAb Abcam ab133288; 1:600; Mouse mAb SCBT sc-48404; 1:200), S9.6 (Sigma MABE1095; 1:150), or NCL (Novus NBP2-44612-0.02mg; 1:500) for 2 hours. The donkey serum, non-confluent cells, 2 hour primary, and day 3 staining is *vital* for visualizing consistent EWSR1 cytoplasmic staining. After incubation with primary antibodies, coverslips were washed three times with PBS. Then coverslips were inverted onto 100 µL of antibody block with secondary antibodies (Alexa Fluor 488 anti-mouse - 1:200, Life Technologies #A11029; Alexa Fluor 594 anti-rabbit – 1:200, Life Technologies A11037) and DAPI (DNA, 1:500 dilution) for 20 minutes in the dark. Coverslips were again washed 3x with PBS, then gently dipped four times into molecular biology-grade water before inversion onto one drop of Fluoro-Gel (with TES Buffer, Electron Microscopy Sciences, #17985-30) then allowed to air-dry in the dark for at least 10 minutes. Slides were

stored at 4˚C until image collection on the LCCC Microscopy & Imaging Shared Resource's Leica SP8 microscope with the 63X oil objective at 1.52 magnification.

DNAse I treatment

Cells were seeded at a density of 25,000-30,000 cells onto 18mm diameter #1.5 round coverslips (VWR, #101413-518) in 12-well dishes (day1). They were allowed to attach to the coverslips for a full day (day2). On the following day (day3), the media was removed, cells were washed 3x with PBS, and then fixed and permeabilized in 3.2% paraformaldehyde (PFA) with 0.2% Triton X-100 in PBS for 3 minutes at room temperature. 10 µL of a 1000 U of DNAse I stock was added to 500 µL of DNAse I buffer on cells for 10 minutes. Cells were washed 3x with PBS and 3.2% PFA with 0.2% Triton X-100 was added again for 5 minutes post-DNAse I treatment. Immunofluorescent staining was completed as stated above.

RNAse H treatment

Cells were seeded at a density of 25,000-30,000 cells onto 18 mm diameter #1.5 round coverslips (VWR, #101413-518) in 12-well dishes (day1). They were allowed to attach to the coverslips for a full day (day2). On the following day (day3), the media was removed, cells were washed 3x with PBS, and then fixed and permeabilized in 3.2% paraformaldehyde (PFA) with 0.2% Triton X-100 in PBS for 3 minutes at room temperature. 2 µL of a 5000 U of RNAse H stock (NEB M0297S) was added to 500 µL of RNAse H buffer on cells for 5 minutes at 45 °C. Cells were washed 3x with PBS and 3.2% PFA with 0.2% Triton X-100 was added again for 5 minutes post-RNAse H treatment. Immunofluorescent staining was completed as stated above.

Evaluation of acrocentric chromosome copy number changes induced by TMZ resistance

As previously published(Tiek et al., 2018), metaphase spreads were prepared using standard protocol(M et al., 2017). Chromosomes were stained with 4',6'-diamindino-2-phenyloindole (DAPI) to determine total chromosome copy number and acrocentric chromosome copy number in each metaphase. Ratios of total chromosome number to acrocentric chromosome number in each metaphase were calculated and graphed in R.

NanoBRET measurements for GW807982X (CLK2i)

CLK1, 2, and 4 NanoBRET assays were performed as previously described(Robers et al., 2015; Vasta et al., 2018). In brief the *N*-terminal Nano Luciferase/CLK1 fusion (NL-CLK1) or C-terminal Nano Luciferase/CLK2 fusion (CLK2-NL) or C-terminal Nano Luciferase/CLK4 fusion (CLK4-NL) was

encoded in pFN31K expression vector, including flexible Gly-Ser-Ser-Gly linkers between NL and CLK1,2 or 4 (Promega Madison, WI, USA) (Stoddart et al., 2015). For cellular NanoBRET Target Engagement experiments, the NL-CLK1 or CLK2-NL or CLK4-NL fusion construct was diluted with carrier DNA - pGEM-3Zf(-) (Promega, Madison, WI, USA) at a mass ratio of 1:10 (mass/mass), prior to adding FuGENE HD (Promega, Madison, WI, USA). DNA:FuGENE complexes were formed at a ratio of 1:3 (µg DNA/µL FuGENE HD) according to the manufacturer's protocol (Promega, Madison, WI, USA). The resulting transfection complex (1 part, volume) was then gently mixed with 20 parts (v/v) of HEK-293 cells (ATCC) suspended at a density of 2 x 10^5 cells/mL in DMEM (Gibco) + 10% FBS (Seradigm/VWR). 100 µL of this solution was added to each well of a 96-well plate (Corning 3917) followed by incubation (37 °C/ 5 % CO_2) for 24 hours. After 24 hours the media was removed from the HEK293 CLK (NL-CLK1, CLK2-NL or CLK4-NL) transfected cells and replaced with 85 µL OPTI-MEM media (Gibco). NanoBRET Tracer 5 (Promega, Madison, WI, USA) was used at a final concentration of 1.0 µM as previously evaluated in a titration experiment. A total of 5 µL/well (20x working stock of nanoBRET Tracer 5 [20 µM]) was added to all wells, except the "no tracer" control wells to which 5 µL/well of tracer dilution buffer alone was added. All inhibitors were prepared initially as concentrated stock solutions in 100% DMSO (Sigma). A total of 10 µL/well of the 10x chemical inhibitor stock solutions (final assay concentration 1 % DMSO) were added. For "no compound" and "no tracer" control wells, a total of 10 µL /well of Opti-MEM plus DMSO (9 µL was added (final concentration 1 % DMSO)). 96 well plates containing cells with NanoBRET Tracer 5 and inhibitors (100 µL total volume per well) were equilibrated (37 °C/ 5 % CO_2) for 2 hours. To measure NanoBRET signal, NanoBRET NanoGlo substrate at a ratio of 1:166 to Opti-MEM media in combination with extracellular NanoLuc Inhibitor diluted 1:500 (10 µL [30 mM stock] per 5 mL Opti-MEM plus substrate) were combined to create a 3x stock. A total of 50 µL of the 3x substrate/extracellular NanoLuc inhibitor were added to each well. The plates were read within 15 minutes (GloMax Discover luminometer, Promega, Madison, WI, USA) equipped with 450 nM BP filter (donor) and 600 nM LP filter (acceptor), using 0.3 s integration time instrument utilizing the "nanoBRET 618" protocol. Eleven concentrations of GW807982X were evaluated in competition with NanoBRET Tracer 5 in HEK293 cells transiently expressing CLK1, 2, and 4. Prior to curve fitting the values are converted to mBRET units (x1000). Additional normalization of the NanoBRET assay data was performed by converting experimental values for respective concentrations of experimental inhibitors to relative percent control values (no compound [Opti-MEM + DMSO + Tracer 5 only] wells = 100 % Control, no tracer [Opti-MEM + DMSO] wells = 0 % Control). The data was normalized to 0 % and 100 % inhibition control values and

fitted to a four parameter dose-response binding curve in GraphPad Software (version 7, La Jolla, CA, USA).

Cell cycle analysis

For TMPyP4 treatment, on day 0 cells were seeded at 100,000 cells per well in 6-well plastic tissue culture dishes one day prior to treatment with the indicated concentrations of drug. 50 µM TMPyP4 was added on day1, treatment time was 48 hours. After 48 hours, cells were collected, washed with PBS, ethanol-fixed, stained with propidium iodide, and analyzed for cell subG1 (fragmented/apoptotic) DNA content and cell cycle profile. 20,000 cells were acquired by flow cytometry on a Becton Dickinson Fortessa. Files were modeled using ModFit software (Verity Software, Topsham, ME) to determine subG1, G1, S, and G2/M cell cycle stage. For CLK2i treatment, on day 0 cells were seeded at 200,000 cells per well in 6-well plastic tissue culture dishes one day prior to treatment with the indicated concentrations of drug. 5 µM CLK2i was added on day1, treatment time was 24 hours. After 24 hours, cells were collected, washed with PBS, ethanol-fixed, stained with propidium iodide, and analyzed for cell subG1 (fragmented/apoptotic) DNA content, cell cycle profile, and growth rate. 20,000 cells were acquired by flow cytometry on a Becton Dickinson Fortessa. Files were modeled using ModFit software (Verity Software, Topsham, ME) to determine subG1, G1, S, and G2/M cell cycle stage.

Nucleolar size and circularity detection and graphing

Images taken from the Leica SP8 microscope were opened in FIJI, split into the channel to be analyzed, and converted from RGB to 8-bit images for analysis. In FIJI, the intensity threshold was set via Image -> Adjust -> Threshold (over/under 95). Next, the image was made into a binary form (Process -> Binary -> Make binary). Finally, particles that met the threshold were quantified for area and circularity via Analyze -> Analyze particles. These readouts were then imported into R and graphed/analyzed using the R markdown file “Raincloud_Area” in the supplemental files.

Western blot analysis

Cells were lysed in RIPA buffer supplemented with protease and phosphatase inhibitors (Roche, #4906837001) for protein extractions and separated by polyacrylamide gel electrophoresis using 4-12% gradient gels (Novex by Life Tech, #NP0321BOX) as described previously (19). They were then transferred onto Nitrocellulose membranes (Invitrogen, #IB23001) with the iBlot2 (Invitrogen, #IB21001) and probed with the following antibodies: EWSR1 (1:1000, abcam, ab133288), CLK2 (1:1000, sigma, HPA055366-100UL), phosphorylated SR proteins (clone 1H4, 1:500, Millipore,

#MABE50. Beta-Tubulin (1:5000, Sigma Aldrich, #T7816) and Beta-Actin (1:5000, Sigma-Aldrich, #A5316) were used as loading controls. Proteins were detected with horseradish peroxidase-conjugated secondary antibodies (1:5000, GE Healthcare Life Sciences, #NA931-1ML (Mouse) or #NA934-1ML (Rabbit)) and enhanced chemiluminescent detection HyGLO Quick Spray Chemiluminescent (Denville Scientific, #E2400) using film (Denville Scientific, #E3212).

High resolution stimulated emission depletion microscopy (STED)

STED images were acquired using a Leica SP8 3X STED microscope, a white-light laser for fluorescence excitation (470-670 nm), time-gated hybrid-PMTs, and a Leica 100x (1.4 N.A.) STED White objective (Leica Microsystems, Inc.). AF594 was excited with 575nm excitation, with a back projected pinhole at 200 nm, and the fluorescence emission was collected at 610 nm with a Line average or 4, Frame accumulation of 2, and Line accumulation of 1. Time-gating of the emission signal from the PMT was set to a range of 0.7-6.5 ns for experiments involving the 775 nm depletion laser. Z-stacks were taken X= 24.890 nm, Y=24.890 nm, and Z=160.217 nm. The pinhole was set to a value of 0.7 airy units for all images. Image deconvolution was performed using Hyugens software (Scientific Volume Imaging B.V., Netherlands) assuming an idealized STED point spread function.

siRNA knockdown of EWSR1

Dharmacon individual set of 4 2 nmol EWSR1 siRNAs were purchased (LQ-005119-02-0002) and resuspended in RNA reconstitution buffer provided. On day 0, 250 µL of Opti-MEM was warmed and added to 5 µL of siRNA (stock = 20 µM) and 7.5 µL of Trans-IT X2. The mixture was left to form micelles for 25 minutes. This was then added dropwise to 6-wells with 1% FBS media and 100,000 freshly plated cells. The cells then adhered overnight, and media was changed the following morning. Cells were collected 48 hours later for either cell cycle analysis or Western blot, which allowed for 72 hours of transfection total.

Immunohistochemistry on human GBM patient samples

Immunohistochemical staining of GBM was performed for EWSR1. Five-micron sections from formalin fixed paraffin embedded tissues were de-paraffinized with xylenes and rehydrated through a graded alcohol series. Heat induced epitope retrieval (HIER) was performed by immersing the tissue sections at 98 °C for 20 minutes in 10 mM citrate buffer (pH 6.0) with 0.05% Tween. Immunohistochemical staining was performed using a horseradish peroxidase labeled polymer from Agilent (K4003) according to manufacturer's instructions. Briefly, slides were treated with 3% hydrogen peroxide and 10% normal

goat serum for 10 minutes each and exposed to primary antibodies for EWSR1 (1/400, Abcam, ab133288) overnight at 4 °C. Slides were exposed to the appropriate HRP labeled polymer for 30 min and DAB chromagen (Dako) for 5 minutes. Slides were counterstained with Hematoxylin (Fisher, Harris Modified Hematoxylin), blued in 1% ammonium hydroxide, dehydrated, and mounted with Acrymount. Consecutive sections with the primary antibody omitted were used as negative controls.

RNA isolation

750,000 cells were seeded on day 0. The following day cells were washed 3x with PBS, trypsinized, and pelleted into an Eppendorf tube. Then, 4 mL of TRIzol was added to each tube and incubated at room temperature for 5 minutes. 1 mL of each sample was aliquoted into 4 separate tubes. 200 µL of chloroform was added to each tube and vortexed briefly to mix. Samples incubated at room temperature for 5 minutes, were briefly vortexed, and then centrifuged at 12,000g for 10 min at 4 °C. 500 µL of the clear upper layer was collected from each tube and pooled into two 1 mL Eppendorf tubes where 500 µL of isopropanol was added and mixed thoroughly by multiple inversions. Samples were incubated for 15 minutes at room temperature, and then centrifuged for 15 minutes at 12,000 g at 4 °C. Supernatant was then discarded, and pellet was washed with 750 µL 80% ethanol by multiple inversions. Sample was centrifuged for 5 minutes at 4 °C at 12,000 g. Pellet was again washed with 80% ethanol by multiple inversions and centrifuged the same way as before. The supernatant was removed and discarded, and a second quick spin was done to remove any residual contaminating liquid. The RNA pellet was then air dried for 10 minutes before being resuspended in 100 µL of nuclease-free water. Total RNA was quantified using a NanoDrop 2000.

Nanopore sequencing

20 µg aliquots of total RNA were diluted in 100 µl of nuclease free water and poly-A selected using NEXTflex Poly(A) Beads (BIOO Scientific Cat#NOVA-512980). Resulting poly-A RNA was quantified and 50 ng aliquots were transferred to thin walled Eppendorf PCR tubes. The biological poly-A RNA and a synthetic control (Lexogen SIRV Set 3, 0.5 ng) were prepared for cDNA synthesis and nanopore sequencing following the ONT SQK-PCS108 kit protocol with a few exceptions. During the reverse transcription step, Superscript IV was used and the reverse transcription incubation time was increased to 15 minutes. After reverse transcription, PCR was performed using LongAmp Taq Master Mix (NEB) under the following conditions: 95ºC for 30 seconds, 10 cycles (95ºC for 15 seconds, 62ºC for 15 seconds, 65ºC for 15 minutes), 65ºC for 15 minutes, hold at 4ºC. The resulting cDNA libraries were quantified and sequencing libraries were prepared using 700 ng of cDNA following the standard

protocol for SQK-PCS108 (1D sequencing). Sequencing was performed on the GridION platform using ONT R9.4 flow cells and the standard MinKNOW protocol script (NC_48hr_sequencing_FLO-MIN106_SCK-PCS108).

Nanopore full-length sequencing analysis

Albacore workflow (version 2.1.3) was used for basecalling cDNA data. Using minimap2(Li, 2018) with recommended parameters (-ax splice -uf -k14), reads were aligned to the GRCh38 human genome reference[2] in order to investigate possible novel isoforms. To define isoforms from the sets of cDNA reads, we used FLAIR (v1.3)(Tang et al.). Using FLAIR-correct, we corrected the aligned reads providing splice site evidence from Gencode v29(Frankish et al., 2019) annotations. The corrected and filtered reads were then given to FLAIR-collapse to produce a nanopore-specific reference containing high-confidence isoforms with at least 3 supporting reads. FLAIR-quantify was then used to quantify FLAIR isoform usage across different samples. SUPPA2(Trincado et al., 2018), a differential splicing analysis tool was used to investigate different local alternative splicing event types across samples. Files and codes associated with this analysis can be found at https://github.com/timplab/Drug_resistant_GBM.

DNA isolation for Whole genome sequencing

750,000 cells were collected for each cell line, where DNA was isolated using the DNeasy Blood and Tissue Kit (Qiagen; Cat. No. 69504). Briefly, cells were centrifuged and resuspended with proteinase K and buffer AL for 10 min at 56 ℃. 200 µL of ethanol was then added and mixed thoroughly by vortexing. DNA was added to the DNeasy Mini spin column, centrifuged, and flow-through discarded. DNA was washed in the DNeasy column with buffer AW1 once, and AW2 once as well. Membrane was then dried by centrifugation with all flow-through being discarded. DNA was eluted using 200 µL buffer AE after 1 min incubation at room temperature.

Whole genome sequencing using Illumina TruSeq DNA PCR-Free Library prep Kit

Illumina TruSeq DNA PCR-Free Library prep Kit was used per manufactures instructions. Paired-end, indexed libraries for human whole genome sequencing were constructed from 1.0 µg gDNA using the TruSeq DNA PCR-Free Library Prep Kit (Illumina, San Diego) according to manufacturer's instructions. Briefly, DNA was fragmented using a Covaris M220 focused ultrasonicator (Covaris, Woburn, MA) using settings for a 350 bp insert size. Library quality was assessed with a BioAnalyzer 2100 using the High Sensitivity DNA kit (Agilent Technologies, Santa Clara, CA). The libraries were quantified using the Kapa Library Quantification Kit Illumina Platforms (Kapa Biosystems, Boston,

MA). The denatured and diluted libraries were sequenced on a NextSeq 550 System (Illumina) using v2.5 High Output 300 cycle kit with 1% PhiX to an average sequencing depth of 50X coverage.

Whole genome sequencing analysis

Raw data were first demultiplexed into 3 groups, which were 42MBGA-WT, 42MGBA-TMZres and T98G, each group had two biological duplicates. All raw sequence data (fastq files) were run through fastQC v0.11.7 for quality check, lower quality reads (Q < 20) were eliminated. Cutadapt v2.1 was used for adapter trimming, read length less than 20 bp after trimming were filtered. Processed reads were then aligned to GRCh38 reference sequence using bwa v0.7.17 paired-end mode(Li and Durbin, 2009). Mutation detection was conducted in GATK v4.1.0.0(McKenna et al., 2010) following the best practice for variant calling workflow(DePristo et al., 2011). The consensus assembly for each sample were created by bcftools, then the Quadron methodology(Sahakyan et al., 2017) was used to detect stable G4 structures. Unique G-Quad sequence with Q > 19 were extracted from each group for further analysis

Data availability

The whole genome DNA sequencing and Nanopore full-length RNA sequencing raw data generated and analysed in the current study are available from the corresponding authors upon request, and will be deposited to the NCBI Sequence Read Archive prior to publication.

Figure Legends

Figure 1. Guanine mutations in TMZ-resistant GBM cells disrupt G-quadruplex (G4) structure and associate with sensitivity to the G4 stabilizing drug TMPyP4. a. Single nucleotide changes identified by whole genome sequencing data aligned to GRCh38 and analyzed by Genome Analysis Toolkit (GATK) mutation calling; duplicate samples with 2-way ANOVA for total mutation count. b. Enrichment of G>A and C>T transition mutations in TMZ-resistant cells; duplicate samples with 2-way ANOVA. c. MEME-predicted enriched motifs from Quadron-derived unique acrocentric chromosome sequences between 42MBGA(E-value top; 1.4e-231, bottom; 9.4e-013), 42MBGA-TMZres (E-value 7.9e-206), and T98G (E-value top; 9.3e-198, bottom; 7.2e-013) cell lines. d-g. Immunofluorescent staining with the G-quadruplex antibody BG4 in d. TMZ-sensitive 42MBGA, e. 72 hr-treated 42MBGA, and TMZ-resistant f. 42MBGA-TMZres, and g. T98G cells with surface plots of signal intensity below generated by FIJI. Yellow outline denotes nuclear BG4 staining and the region analyzed in FIJI; representative of three biological replicates. h. Graphical depiction of the hypothesis that TMZ-induced O6-methylguanine (O^6meG) adducts and subsequent mutations disrupt G4s. i-k. FACS analysis following 24 hours of treatment with 50 µM TMPyP4 or DMSO vehicle control in 42MBGA, 42MBGA-TMZres, and T98G cells; three biological replicates. i. Growth rates; t-test. j. Percent of cells in G2/M; t-test. k. Percent of cells with subG1 DNA content; t-test * $p<0.05$, ** $p<0.001$ *** $p<0.0005$, **** $p<0.0001$.

Figure 2. TMZ treatment and resistance associate with increased nucleolar stress and the formation of nucleolar R-loops. a. Analysis of acrocentric chromosome fraction between 42MBGA and 42MBGA-TMZres from total chromosome metaphase spreads. b. Representative images of endogenous nucleolin (NCL) immunofluorescence (IF). c. Quantification of nucleolar area from images in b. d. Quantification of nucleolar circularity from images in b. IF with the R-loop binding S9.6 antibody in e. 42MBGA, f. 72 hr TMZ treatment in 42MGBA, g. 42MBGA-TMZres, h. T98G. i. Quantification of R-loop intensity in e, g and h. ** $p<0.005$, **** $p<0.0001$.

Figure 3. Splice-site mutations in TMZ-resistant GBM cells associate with increased exon skipping and sensitivity to a novel CLK inhibitor (GW807982X, CLK2i). a. Quantification of splice-site mutations in TMZ-sensitive vs. -resistant cells from whole genome sequencing analyses described in Figure 1; One-way ANOVA. b. FLAIR and SUPPA2 analysis of Oxford Nanopore Technology full-length transcript sequencing for differences in alternative splicing by event type in TMZ-sensitive 42MGBA and TMZ-resistant 42MGBA-TMZres and T98G cells. c. Quantified IF of pSR (1H4) intensity

in cells with (γH2AX+) or without (γH2AX-) DNA damage; two-tailed t-test. d. Association between CLK2 mRNA expression and overall survival in the REMBRANDT brain cancer data set; log-rank (Mantel-Cox) test. e. Association between CLK2 expression and increasing brain tumor grade and aggressiveness in the REMBRANDT dataset; one-way ANOVA. f. Western blot of CLK2 expression in TMZ-sensitive, -treated, and -resistant GBM cell lines. g. FACS analysis for cell cycle profile in response to 5 μM CLK2i vs. DMSO vehicle control treatment for 24 hours; three biological replicates with One-way ANOVA. h. Relative cell numbers following 24 hr treatment with 5 μM CLK2i vs DMSO vehicle control; three biological replicates with t-test, i. SubG1 or apoptotic DNA content in cells analyzed in g; three biological replicates with t-test. * $p<0.05$, ** $p<0.001$, *** $p<0.0005$, **** $p<0.0001$.

Figure 4. The RNA binding protein EWSR1 forms cytoplasmic, amyloid-like aggregates in TMZ-treated and TMZ-resistant GBM cells. a. Basal IF of EWSR1 in the indicated cell lines, with the nucleus outlined in yellow. High-resolution stimulated emission depletion microscopy (STED) imaging of EWSR1 cytoplasmic aggregates in b. 42MBGA-TMZres and c. T98G cells. d. Western blot of EWSR1 total protein expression in the indicates cell lines. e. Localization of EWSR1 to nucleoli adjacent to R-loops (S9.6) following 3 hr 10nM Actinomycin D (ActD) treatment to inhibit RNAPI. STED imaging of EWSR1 nucleolar movement following 3 hr ActD treatment in f. 42MBGA, g. 42MBGA-TMZres, h. T98G cells.

Figure 5. Cytoplasmic EWSR1 aggregates are detected in GBM clinical specimens. a. Characteristics of GBM patients with outer circle denoting age, middle circle denoting sex, and inner circle denoting EWSR1 aggregate status. b. IHC of EWSR1 in 6 GBM patient samples. Red box denotes higher magnification inset showing cells with cytoplasmic aggregates of EWSR1.

Financial Support: This work was supported by a Georgetown University Medical Center (GUMC) Dean for Research's Toulmin Pilot Project Award (RBR), and a Partners in Research Breakthrough Award (RBR), as well as F99 CA234799 (DMT) and a student research grant from the Medical Center Graduate Student Organization (MCGSO, to DMT). Additional fellowship funding for DMT was provided by the Tumor Biology Training Grant (T32 CA009686, PI: Dr. Anna T. Riegel). Technical services were provided by the GUMC, Flow Cytometry & Cell Sorting, Histopathology & Tissue, Microscopy & Imaging, and Tissue Culture Shared Resources, which are supported in part by Cancer Center Support Grant P30 CA051008 (PI: Dr. Louis M. Weiner). The content of this article is the sole responsibility of the authors and does not represent the official views of the National Institutes of Health.

Conflict of Interest and Author Contribution Statement: The authors declare no potential conflict of interest. DMT contributed to study design, performed experiments, analyzed data, and wrote the paper. RR analyzed data. NS performed experiments. LJ analyzed data. CAF performed experiments. JRH provided reagents and input on the paper. BRH performed experiments and input on the paper. DHD provided reagents and input on the paper. CIW performed experiments. JEP performed experiments. WJZ contributed to study design, provided reagents, and input on the paper. WT contributed to study design, provided reagents, and input on the paper. RBR contributed to study design, analyzed data, and wrote the paper. All authors reviewed, edited, and approved the manuscript.

Acknowledgements

We wish to thank Drs. Deborah Berry, Angela Brooks, Christian Combs, Karen Creswell, Brent Harris, Rong Hu, Peter Johnson, Moshe Levi, Supti Sen, Alexandra Taraboletti, Jeffrey Toretsky, Todd Waldman, Cameron Soulette, Jay Patel and Dan Xun for sharing reagents, scientific insights, technical assistance, and/or editorial comments on the manuscript.

References

Agarwal, S., Kern, S., Halbert, J., Przyborski, J.M., Baumeister, S., Dandekar, T., Doerig, C., and Pradel, G. (2011). Two nucleus-localized CDK-like kinases with crucial roles for malaria parasite erythrocytic replication are involved in phosphorylation of splicing factor. J. Cell. Biochem. *112*, 1295–1310.

Alexandrov, L.B., Nik-Zainal, S., Wedge, D.C., Aparicio, S.A.J.R., Behjati, S., Biankin, A.V., Bignell, G.R., Bolli, N., Borg, A., Børresen-Dale, A.-L., et al. (2013). Signatures of mutational processes in human cancer. Nature *500*, 415–421.

Bacolla, A., Temiz, N.A., Yi, M., Ivanic, J., Cer, R.Z., Donohue, D.E., Ball, E.V., Mudunuri, U.S., Wang, G., Jain, A., et al. (2013). Guanine holes are prominent targets for mutation in cancer and inherited disease. PLoS Genet. *9*, e1003816.

Bailey, T.L., and Elkan, C. (1994). Fitting a mixture model by expectation maximization to discover motifs in biopolymers. Proc Int Conf Intell Syst Mol Biol *2*, 28–36.

Balasubramanian, S., Hurley, L.H., and Neidle, S. (2011). Targeting G-quadruplexes in gene promoters: a novel anticancer strategy? Nat Rev Drug Discov *10*, 261–275.

Bejar, R. (2016). Splicing Factor Mutations in Cancer. Adv. Exp. Med. Biol. *907*, 215–228.

Bernat, V., and Disney, M.D. (2015). RNA Structures as Mediators of Neurological Diseases and as Drug Targets. Neuron *87*, 28–46.

Biffi, G., Tannahill, D., McCafferty, J., and Balasubramanian, S. (2013). Quantitative visualization of DNA G-quadruplex structures in human cells. Nat Chem *5*, 182–186.

Braun, C.J., Stanciu, M., Boutz, P.L., Patterson, J.C., Calligaris, D., Higuchi, F., Neupane, R., Fenoglio, S., Cahill, D.P., Wakimoto, H., et al. (2017). Coordinated Splicing of Regulatory Detained Introns within Oncogenic Transcripts Creates an Exploitable Vulnerability in Malignant Glioma. Cancer Cell *32*, 411–426.e411.

Bravaya, K.B., Kostko, O., Dolgikh, S., Landau, A., Ahmed, M., and Krylov, A.I. (2010). Electronic structure and spectroscopy of nucleic acid bases: ionization energies, ionization-induced structural changes, and photoelectron spectra. J Phys Chem A *114*, 12305–12317.

Cheung-Ong, K., Giaever, G., and Nislow, C. (2013). DNA-damaging agents in cancer chemotherapy: serendipity and chemical biology. Chem. Biol. *20*, 648–659.

Cogoi, S., and Xodo, L.E. (2006). G-quadruplex formation within the promoter of the KRAS proto-oncogene and its effect on transcription. Nucleic Acids Res. *34*, 2536–2549.

Cui, B., Johnson, S.P., Bullock, N., Ali-Osman, F., Bigner, D.D., and Friedman, H.S. (2010). Decoupling of DNA damage response signaling from DNA damages underlies temozolomide resistance in glioblastoma cells. J Biomed Res *24*, 424–435.

De Vleeschouwer, S., Fernandes, C., Costa, A., Osório, L., Lago, R.C., Linhares, P., Carvalho, B., and Caeiro, C. (2017). Current Standards of Care in Glioblastoma Therapy. Glioblastoma 197–241.

DePristo, M.A., Banks, E., Poplin, R., Garimella, K.V., Maguire, J.R., Hartl, C., Philippakis, A.A., del Angel, G., Rivas, M.A., Hanna, M., et al. (2011). A framework for variation discovery and genotyping using next-generation DNA sequencing data. Nat. Genet. *43*, 491–498.

Drewry, D.H., Willson, T.M., and Zuercher, W.J. (2014). Seeding collaborations to advance kinase science with the GSK Published Kinase Inhibitor Set (PKIS). Curr Top Med Chem *14*, 340–342.

Elkins, J.M., Fedele, V., Szklarz, M., Abdul Azeez, K.R., Salah, E., Mikolajczyk, J., Romanov, S., Sepetov, N., Huang, X.-P., Roth, B.L., et al. (2016). Comprehensive characterization of the Published Kinase Inhibitor Set. Nat. Biotechnol. *34*, 95–103.

Fernando, H., Reszka, A.P., Huppert, J., Ladame, S., Rankin, S., Venkitaraman, A.R., Neidle, S., and Balasubramanian, S. (2006). A conserved quadruplex motif located in a transcription activation site of the human c-kit oncogene. Biochemistry *45*, 7854–7860.

Frankish, A., Diekhans, M., Ferreira, A.-M., Johnson, R., Jungreis, I., Loveland, J., Mudge, J.M., Sisu, C., Wright, J., Armstrong, J., et al. (2019). GENCODE reference annotation for the human and mouse genomes. Nucleic Acids Res. *47*, D766–D773.

Fujiwara, N., Mazzola, M., Cai, E., Wang, M., and Cave, J.W. (2015). TMPyP4, a Stabilizer of Nucleic Acid Secondary Structure, Is a Novel Acetylcholinesterase Inhibitor. PLoS ONE *10*, e0139167.

Gan, W., Guan, Z., Liu, J., Gui, T., Shen, K., Manley, J.L., and Li, X. (2011). R-loop-mediated genomic instability is caused by impairment of replication fork progression. Genes Dev. *25*, 2041–2056.

Gonçalves, V., Pereira, J.F.S., and Jordan, P. (2017). Signaling Pathways Driving Aberrant Splicing in Cancer Cells. Genes (Basel) *9*, 9.

Gorthi, A., Romero, J.C., Loranc, E., Cao, L., Lawrence, L.A., Goodale, E., Iniguez, A.B., Bernard, X., Masamsetti, V.P., Roston, S., et al. (2018). EWS-FLI1 increases transcription to cause R-loops and block BRCA1 repair in Ewing sarcoma. Nature *555*, 387–391.

Grünewald, T.G.P., Bernard, V., Gilardi-Hebenstreit, P., Raynal, V., Surdez, D., Aynaud, M.-M., Mirabeau, O., Cidre-Aranaz, F., Tirode, F., Zaidi, S., et al. (2015). Chimeric EWSR1-FLI1 regulates the Ewing sarcoma susceptibility gene EGR2 via a GGAA microsatellite. Nat. Genet. *47*, 1073–1078.

Haeusler, A.R., Donnelly, C.J., Periz, G., Simko, E.A.J., Shaw, P.G., Kim, M.-S., Maragakis, N.J., Troncoso, J.C., Pandey, A., Sattler, R., et al. (2014). C9orf72 nucleotide repeat structures initiate molecular cascades of disease. Nature *507*, 195–200.

Hanson, K.A., Kim, S.H., and Tibbetts, R.S. (2012). RNA-binding proteins in neurodegenerative disease: TDP-43 and beyond. Wiley Interdiscip Rev RNA *3*, 265–285.

Harrison, A.F., and Shorter, J. (2017). RNA-binding proteins with prion-like domains in health and disease. Biochem. J. *474*, 1417–1438.

Hänsel-Hertsch, R., Di Antonio, M., and Balasubramanian, S. (2017). DNA G-quadruplexes in the human genome: detection, functions and therapeutic potential. Nat. Rev. Mol. Cell Biol. *18*, 279–284.

Izhar, L., Adamson, B., Ciccia, A., Lewis, J., Pontano-Vaites, L., Leng, Y., Liang, A.C., Westbrook, T.F., Harper, J.W., and Elledge, S.J. (2015). A Systematic Analysis of Factors Localized to Damaged Chromatin Reveals PARP-Dependent Recruitment of Transcription Factors. Cell Rep *11*, 1486–1500.

König, F., Schubert, T., and Längst, G. (2017). The monoclonal S9.6 antibody exhibits highly variable binding affinities towards different R-loop sequences. PLoS ONE *12*, e0178875.

Li, H. (2018). Minimap2: pairwise alignment for nucleotide sequences. Bioinformatics *34*, 3094–3100.

Li, H., and Durbin, R. (2009). Fast and accurate short read alignment with Burrows–Wheeler transform. Bioinformatics *25*, 1754–1760.

Lindström, M.S., Jurada, D., Bursac, S., Orsolic, I., Bartek, J., and Volarevic, S. (2018). Nucleolus as an emerging hub in maintenance of genome stability and cancer pathogenesis. Oncogene *37*, 2351–2366.

Luo, Y., Blechingberg, J., Fernandes, A.M., Li, S., Fryland, T., Børglum, A.D., Bolund, L., and Nielsen, A.L. (2015). EWS and FUS bind a subset of transcribed genes encoding proteins enriched in RNA regulatory functions. BMC Genomics *16*, 929.

M, A., H, L., and M, B. (2017). The AGT cytogenetics laboratory manual, 4th edition. Wiley-Blackwell.

Maharana, S., Wang, J., Papadopoulos, D.K., Richter, D., Pozniakovsky, A., Poser, I., Bickle, M., Rizk, S., Guillén-Boixet, J., Franzmann, T.M., et al. (2018). RNA buffers the phase separation behavior of prion-like RNA binding proteins. Science *360*, 918–921.

Mannas, J.P., Lightner, D.D., Defrates, S.R., Pittman, T., and Villano, J.L. (2014). Long-term treatment with temozolomide in malignant glioma. J Clin Neurosci *21*, 121–123.

Marsoner, T., Schmidt, O.P., Triemer, T., and Luedtke, N.W. (2017). DNA-Targeted Inhibition of MGMT. Chembiochem *18*, 894–898.

McKenna, A., Hanna, M., Banks, E., Sivachenko, A., Cibulskis, K., Kernytsky, A., Garimella, K., Altshuler, D., Gabriel, S., Daly, M., et al. (2010). The Genome Analysis Toolkit: a MapReduce framework for analyzing next-generation DNA sequencing data. Genome Res. *20*, 1297–1303.

McRae, E.K.S., Booy, E.P., Padilla-Meier, G.P., and McKenna, S.A. (2017). On Characterizing the Interactions between Proteins and Guanine Quadruplex Structures of Nucleic Acids. J Nucleic Acids *2017*, 9675348–11.

Membrino, A., Cogoi, S., Pedersen, E.B., and Xodo, L.E. (2011). G4-DNA formation in the HRAS promoter and rational design of decoy oligonucleotides for cancer therapy. PLoS ONE *6*, e24421.

Mills, J.D., and Janitz, M. (2012). Alternative splicing of mRNA in the molecular pathology of neurodegenerative diseases. Neurobiol. Aging *33*, 1012.e11–.e24.

Nakamura, T., Okabe, S., Yoshida, H., Iida, K., Ma, Y., Sasaki, S., Yamori, T., Shin-ya, K., Nakano, I., Nagasawa, K., et al. (2017). Targeting glioma stem cells in vivo by a G-quadruplex-stabilizing synthetic macrocyclic hexaoxazole. Sci Rep *7*, 3605.

Naumann, M., Pal, A., Goswami, A., Lojewski, X., Japtok, J., Vehlow, A., Naujock, M., Günther, R., Jin, M., Stanslowsky, N., et al. (2018). Impaired DNA damage response signaling by FUS-NLS mutations leads to neurodegeneration and FUS aggregate formation. Nature Communications *9*, 335.

Nizamutdinov, D., Stock, E.M., Dandashi, J.A., Vasquez, E.A., Mao, Y., Dayawansa, S., Zhang, J., Wu, E., Fonkem, E., and Huang, J.H. (2018). Prognostication of Survival Outcomes in Patients Diagnosed with Glioblastoma. World Neurosurg *109*, e67–e74.

Paronetto, M.P., Miñana, B., and Valcárcel, J. (2011). The Ewing sarcoma protein regulates DNA damage-induced alternative splicing. Mol. Cell *43*, 353–368.

Prados, M.D., Byron, S.A., Tran, N.L., Phillips, J.J., Molinaro, A.M., Ligon, K.L., Wen, P.Y., Kuhn, J.G., Mellinghoff, I.K., de Groot, J.F., et al. (2015). Toward precision medicine in glioblastoma: the promise and the challenges. Neuro-Oncology *17*, 1051–1063.

R, S., WP, M., van den Bent MJ, M, W., B, F., MJ, T., K, B., AA, B., C, M., U, B., et al. (2005). Radiotherapy plus Concomitant and Adjuvant Temozolomide for Glioblastoma. New England Journal of Medicine 987–996.

Robers, M.B., Dart, M.L., Woodroofe, C.C., Zimprich, C.A., Kirkland, T.A., Machleidt, T., Kupcho, K.R., Levin, S., Hartnett, J.R., Zimmerman, K., et al. (2015). Target engagement and drug residence time can be observed in living cells with BRET. Nature Communications *6*, 10091.

Sahakyan, A.B., Chambers, V.S., Marsico, G., Santner, T., Di Antonio, M., and Balasubramanian, S. (2017). Machine learning model for sequence-driven DNA G-quadruplex formation. Sci Rep *7*, 14535.

Sakashita, E., and Endo, H. (2010). SR and SR-related proteins redistribute to segregated fibrillar components of nucleoli in a response to DNA damage. Nucleus *1*, 367–380.

Seiler, M., Yoshimi, A., Darman, R., Chan, B., Keaney, G., Thomas, M., Agrawal, A.A., Caleb, B., Csibi, A., Sean, E., et al. (2018). H3B-8800, an orally available small-molecule splicing modulator, induces lethality in spliceosome-mutant cancers. Nat. Med. *24*, 497–504.

Shepard, P.J., and Hertel, K.J. (2009). The SR protein family. Genome Biol. *10*, 242.

Siddiqui-Jain, A., Grand, C.L., Bearss, D.J., and Hurley, L.H. (2002). Direct evidence for a G-quadruplex in a promoter region and its targeting with a small molecule to repress c-MYC transcription. Proc. Natl. Acad. Sci. U.S.a. *99*, 11593–11598.

Siegel, R.L., Miller, K.D., and Jemal, A. (2019). Cancer statistics, 2019. CA Cancer J Clin *69*, 7–34.

Simone, R., Balendra, R., Moens, T.G., Preza, E., Wilson, K.M., Heslegrave, A., Woodling, N.S., Niccoli, T., Gilbert-Jaramillo, J., Abdelkarim, S., et al. (2018). G-quadruplex-binding small molecules ameliorate C9orf72 FTD/ALS pathology in vitro and in vivo. EMBO Mol Med *10*, 22–31.

Stamatopoulou, V., Parisot, P., De Vleeschouwer, C., and Lafontaine, D.L.J. (2018). Use of the iNo score to discriminate normal from altered nucleolar morphology, with applications in basic cell biology and potential in human disease diagnostics. Nat Protoc *13*, 2387–2406.

Stoddart, L.A., Johnstone, E.K.M., Wheal, A.J., Goulding, J., Robers, M.B., Machleidt, T., Wood, K.V., Hill, S.J., and Pfleger, K.D.G. (2015). Application of BRET to monitor ligand binding to GPCRs. Nat. Methods *12*, 661–663.

Svetoni, F., Caporossi, D., and Paronetto, M.P. (2014). Oxidative stress affects FET proteins localization and alternative pre-mRNA processing in cellular models of ALS. Free Radic. Biol. Med. *75 Suppl 1*, S51.

Svetoni, F., Frisone, P., and Paronetto, M.P. (2016). Role of FET proteins in neurodegenerative disorders. RNA Biol *13*, 1089–1102.

Takahama, K., Kino, K., Arai, S., Kurokawa, R., and Oyoshi, T. (2011). Identification of Ewing's sarcoma protein as a G-quadruplex DNA- and RNA-binding protein. Febs J. *278*, 988–998.

Tang, A.D., Soulette, C.M., van Baren, M.J., bioRxiv, K.H., 2018 Full-length transcript characterization of SF3B1 mutation in chronic lymphocytic leukemia reveals downregulation of retained introns. Biorxiv.org

.

Tavares, F.X., Boucheron, J.A., Dickerson, S.H., Griffin, R.J., Preugschat, F., Thomson, S.A., Wang, T.Y., and Zhou, H.-Q. (2004). N-Phenyl-4-pyrazolo[1,5-b]pyridazin-3-ylpyrimidin-2-amines as potent and selective inhibitors of glycogen synthase kinase 3 with good cellular efficacy. J. Med. Chem. *47*, 4716–4730.

Tentori, L., and Graziani, G. (2009). Recent approaches to improve the antitumor efficacy of temozolomide. Curr. Med. Chem. *16*, 245–257.

Tiek, D.M., Rone, J.D., Graham, G.T., Pannkuk, E.L., Haddad, B.R., and Riggins, R.B. (2018). Alterations in Cell Motility, Proliferation, and Metabolism in Novel Models of Acquired Temozolomide Resistant Glioblastoma. Sci Rep *8*, 7222.

Tiek, D.M., Rone, J.D., Graham, G.T., Pannkuk, E.L., Haddad, B.R., and Riggins, R.B. (2017). Alterations in Cell Motility, Proliferation, and Metabolism in Novel Models of Acquired Temozolomide Resistant Glioblastoma. bioRxiv.

Trincado, J.L., Entizne, J.C., Hysenaj, G., Singh, B., Skalic, M., Elliott, D.J., and Eyras, E. (2018). SUPPA2: fast, accurate, and uncertainty-aware differential splicing analysis across multiple conditions. Genome Biol. *19*, 40.

Vanderbeek, A.M., Rahman, R., Fell, G., Ventz, S., Chen, T., Redd, R., Parmigiani, G., Cloughesy, T.F., Wen, P.Y., Trippa, L., et al. (2018). The clinical trials landscape for glioblastoma: is it adequate to develop new treatments? Neuro-Oncology *20*, 1034–1043.

Vasta, J.D., Corona, C.R., Wilkinson, J., Zimprich, C.A., Hartnett, J.R., Ingold, M.R., Zimmerman, K., Machleidt, T., Kirkland, T.A., Huwiler, K.G., et al. (2018). Quantitative, Wide-Spectrum Kinase Profiling in Live Cells for Assessing the Effect of Cellular ATP on Target Engagement. Cell Chem Biol *25*, 206–214.e211.

899 Wells, C.I., Kapadia, N.R., Couñago, R.M., and Drewry, D.H. (2018). In depth analysis of kinase cross
900 screening data to identify chemical starting points for inhibition of the Nek family of kinases.
901 Medchemcomm *9*, 44–66.

902 Wen, P.Y., and Kesari, S. (2008). Malignant gliomas in adults. N. Engl. J. Med. *359*, 492–507.

903 Zhang, J., Stevens, M.F.G., and Bradshaw, T.D. (2012). Temozolomide: mechanisms of action, repair
904 and resistance. Curr Mol Pharmacol *5*, 102–114.

905

Figure 1

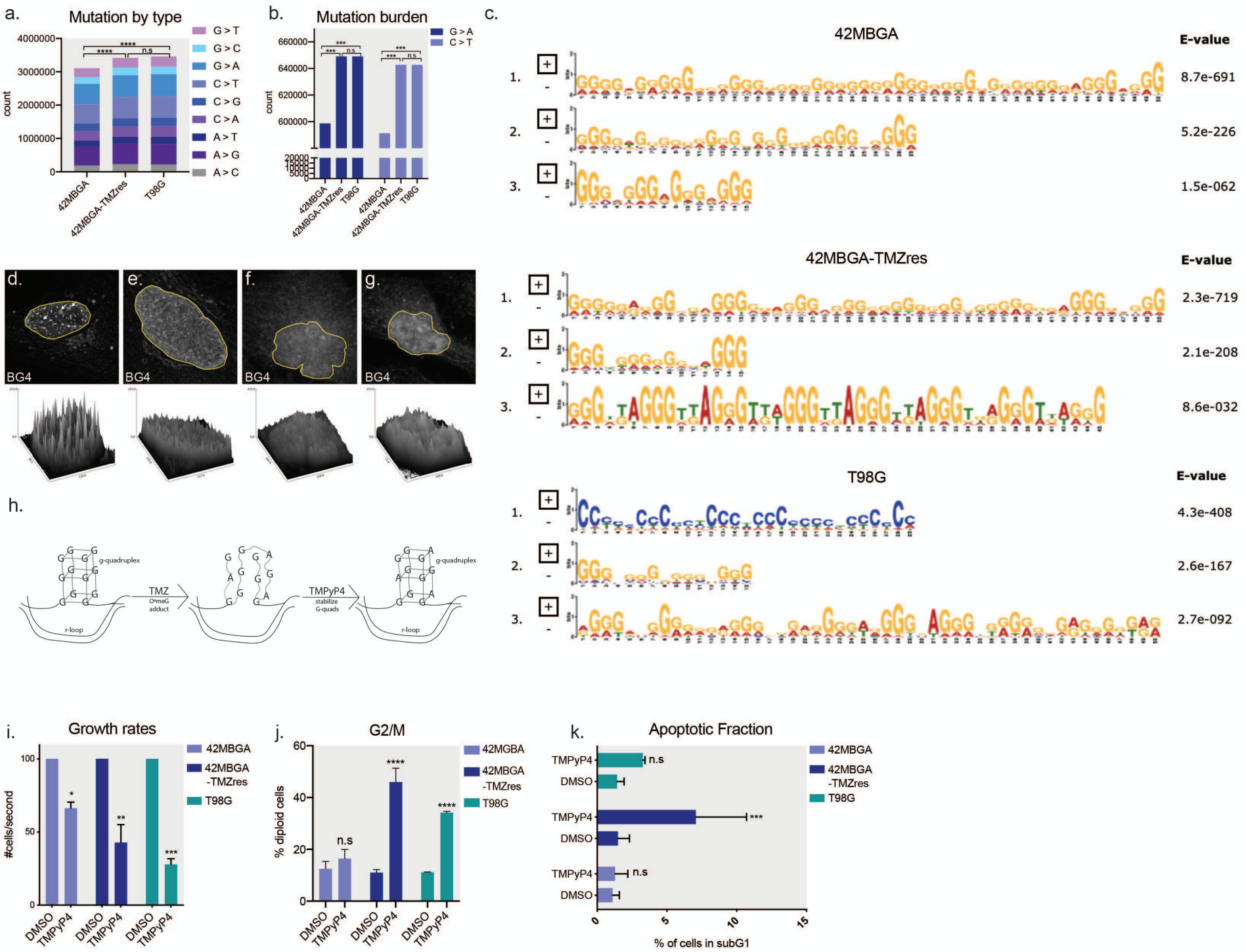
a.
Mutation by type
G > T
G > C
G > A
C > T
C > G
C > A
A > T
A > G
A > C
count
42MBGA
42MBGA-TMZres
T98G
b.
Mutation burden
G > A
C > T
c.
42MBGA
E-value
8.7e-691
5.2e-226
1.5e-062
42MBGA-TMZres
2.3e-719
2.1e-208
8.6e-032
T98G
4.3e-408
2.6e-167
2.7e-092
d.
e.
f.
g.
BG4
h.
g-quadruplex
TMZ
O⁶meG adduct
TMPyP4
stabilize G-quads
r-loop
i.
Growth rates
#cells/second
DMSO
TMPyP4
j.
G2/M
% diploid cells
k.
Apoptotic Fraction
% of cells in subG1
n.s

Figure 2

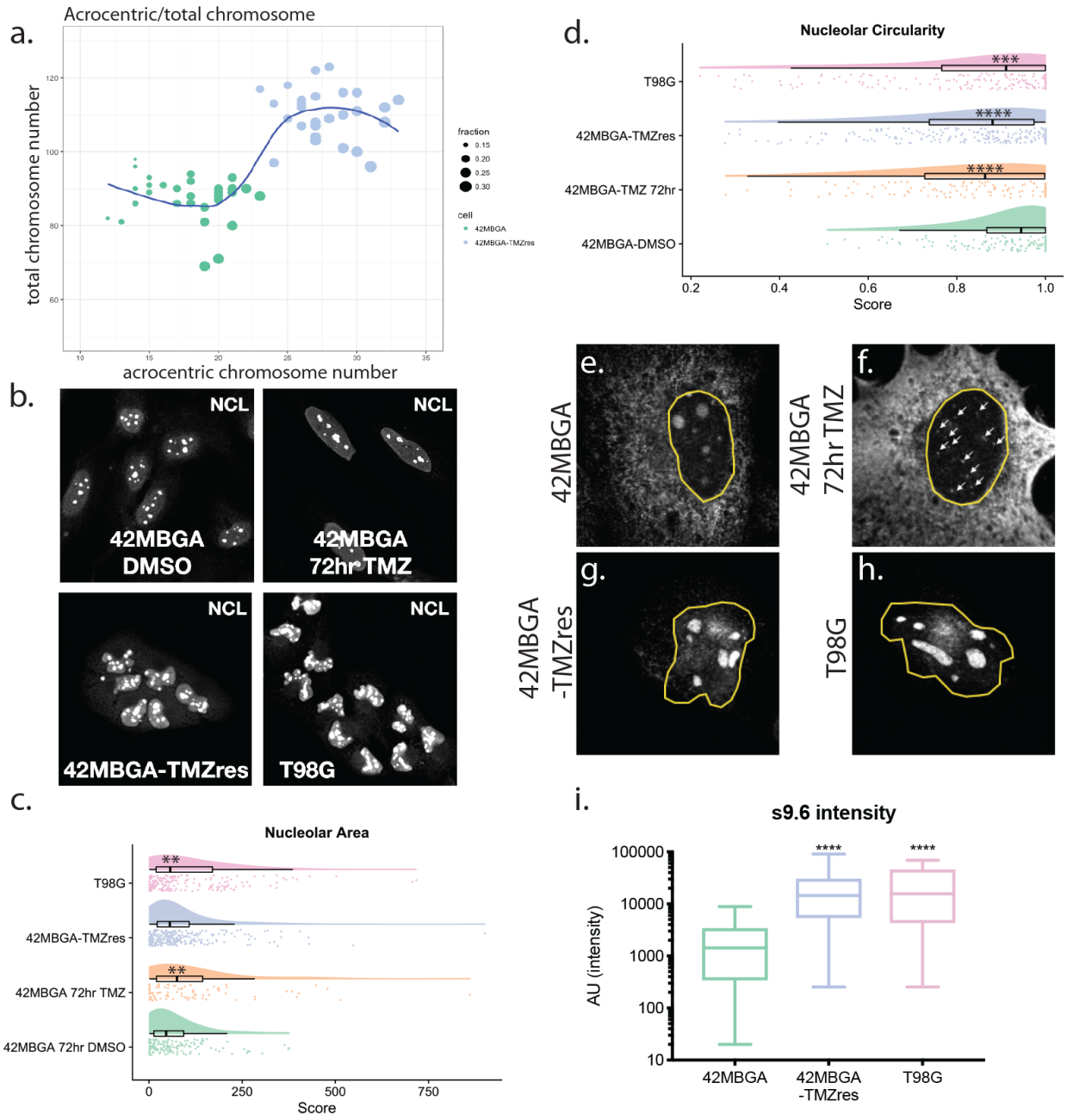
a.
Acrocentric/total chromosome
total chromosome number
acrocentric chromosome number
fraction
cell
42MBGA
42MBGA-TMZres
b.
NCL
42MBGA DMSO
42MBGA 72hr TMZ
42MBGA-TMZres
T98G
c.
Nucleolar Area
T98G
42MBGA-TMZres
42MBGA 72hr TMZ
42MBGA 72hr DMSO
Score
d.
Nucleolar Circularity
T98G
42MBGA-TMZres
42MBGA-TMZ 72hr
42MBGA-DMSO
Score
e.
42MBGA
f.
42MBGA 72hr TMZ
g.
42MBGA -TMZres
h.
T98G
i.
s9.6 intensity
AU (intensity)
42MBGA
42MBGA -TMZres
T98G

Figure 3

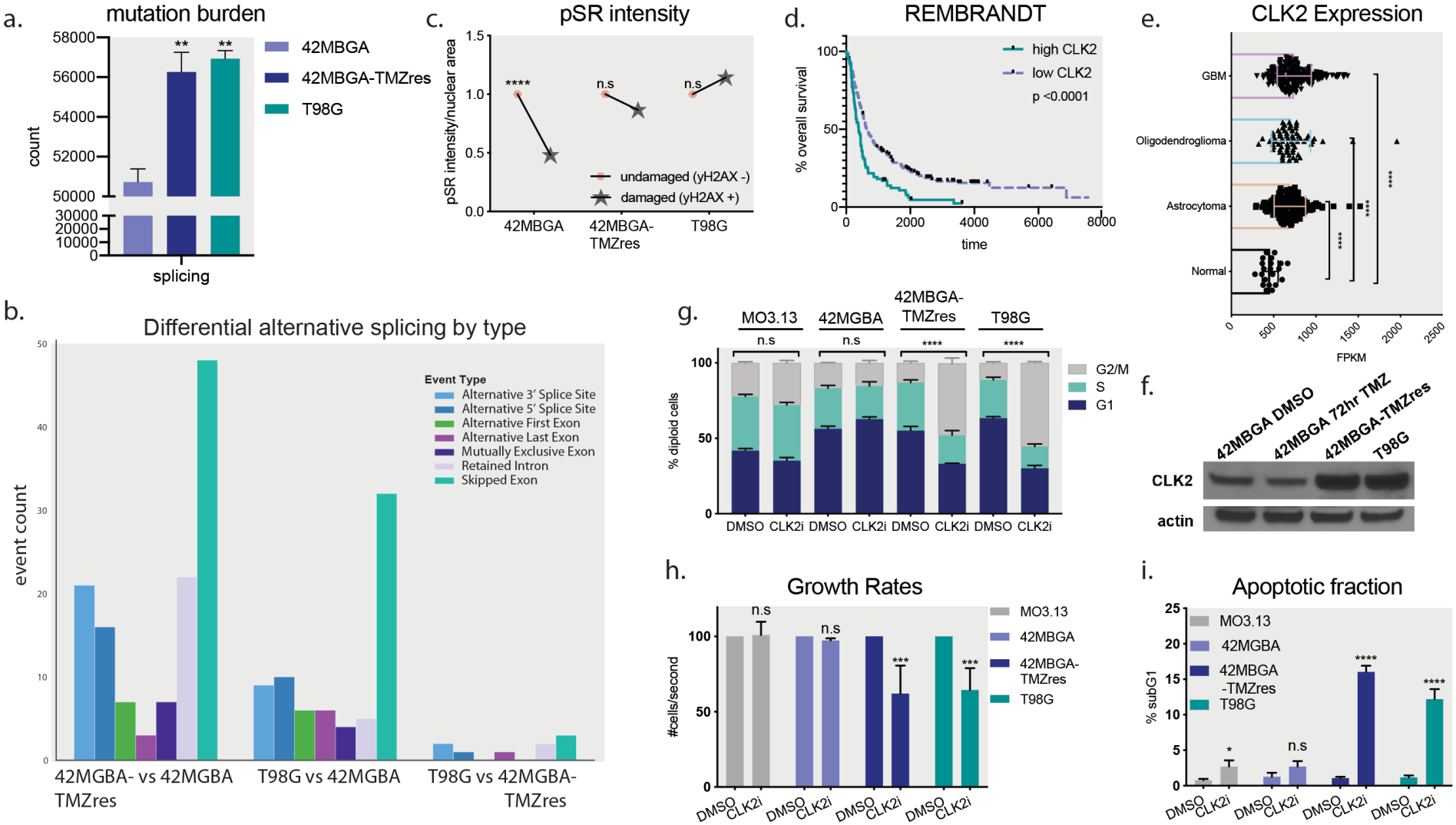
a.
mutation burden
count
splicing
42MBGA
42MBGA-TMZres
T98G
c.
pSR intensity
pSR intensity/nuclear area
undamaged (γH2AX -)
damaged (γH2AX +)
42MBGA
42MBGA-TMZres
T98G
d.
REMBRANDT
% overall survival
high CLK2
low CLK2
p <0.0001
time
e.
CLK2 Expression
GBM
Oligodendroglioma
Astrocytoma
Normal
FPKM
b.
Differential alternative splicing by type
event count
Event Type
Alternative 3′ Splice Site
Alternative 5′ Splice Site
Alternative First Exon
Alternative Last Exon
Mutually Exclusive Exon
Retained Intron
Skipped Exon
42MGBA- vs 42MGBA TMZres
T98G vs 42MGBA
T98G vs 42MGBA-TMZres
g.
MO3.13
42MGBA
42MBGA-TMZres
T98G
% diploid cells
G2/M
S
G1
DMSO CLK2i
f.
42MBGA DMSO
42MBGA 72hr TMZ
42MBGA-TMZres
T98G
CLK2
actin
h.
Growth Rates
#cells/second
MO3.13
42MBGA
42MBGA-TMZres
T98G
i.
Apoptotic fraction
% subG1
MO3.13
42MBGA
42MBGA-TMZres
T98G

Figure 4

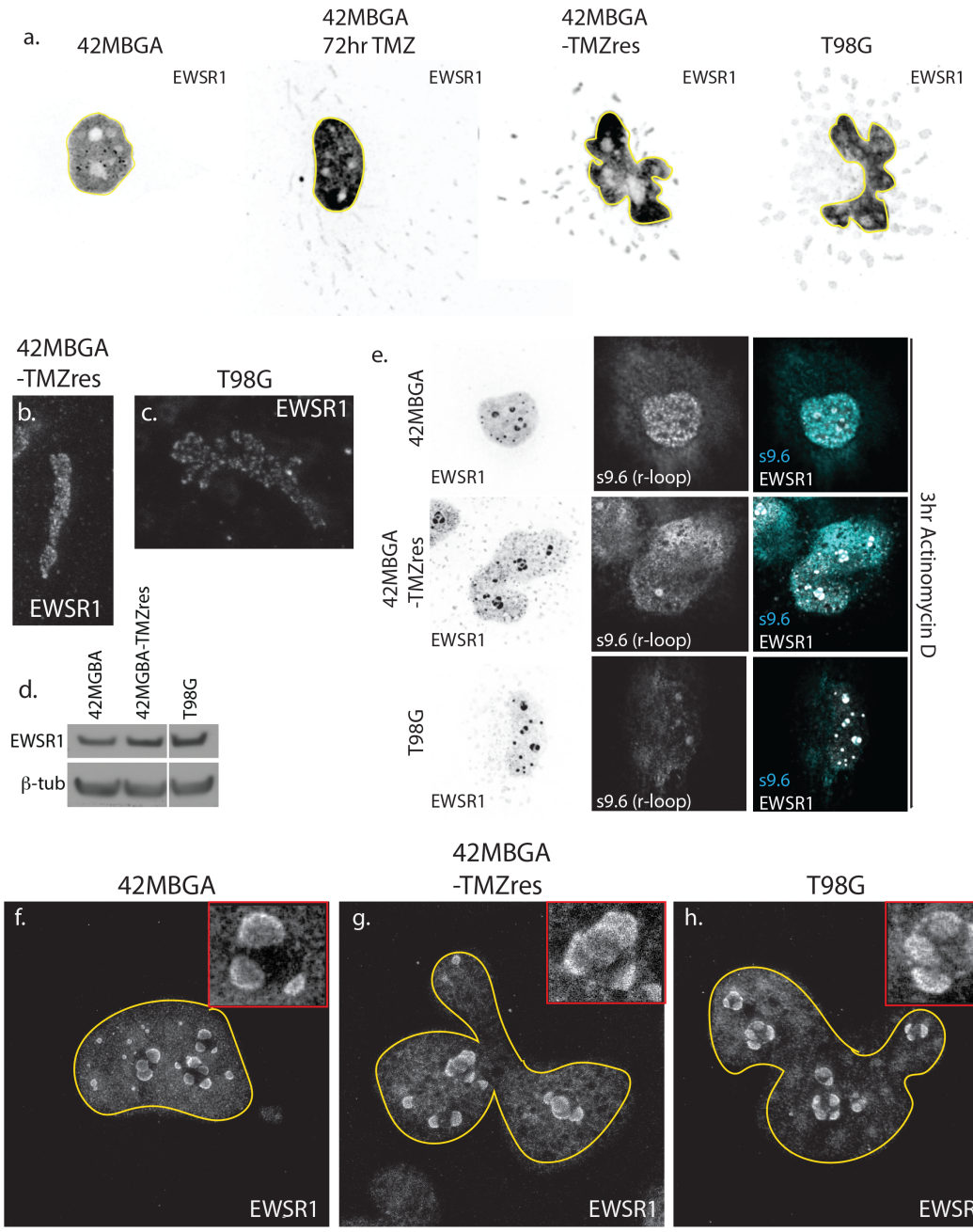
a.
42MBGA
EWSR1
42MBGA
72hr TMZ
EWSR1
42MBGA
-TMZres
EWSR1
T98G
EWSR1
42MBGA
-TMZres
b.
EWSR1
T98G
c.
EWSR1
d.
42MGBA
42MGBA-TMZres
T98G
EWSR1
β-tub
e.
42MBGA
EWSR1
s9.6 (r-loop)
s9.6
EWSR1
42MBGA
-TMZres
EWSR1
s9.6 (r-loop)
s9.6
EWSR1
T98G
EWSR1
s9.6 (r-loop)
s9.6
EWSR1
3hr Actinomycin D
42MBGA
f.
EWSR1
42MBGA
-TMZres
g.
EWSR1
T98G
h.
EWSR1

Figure 5

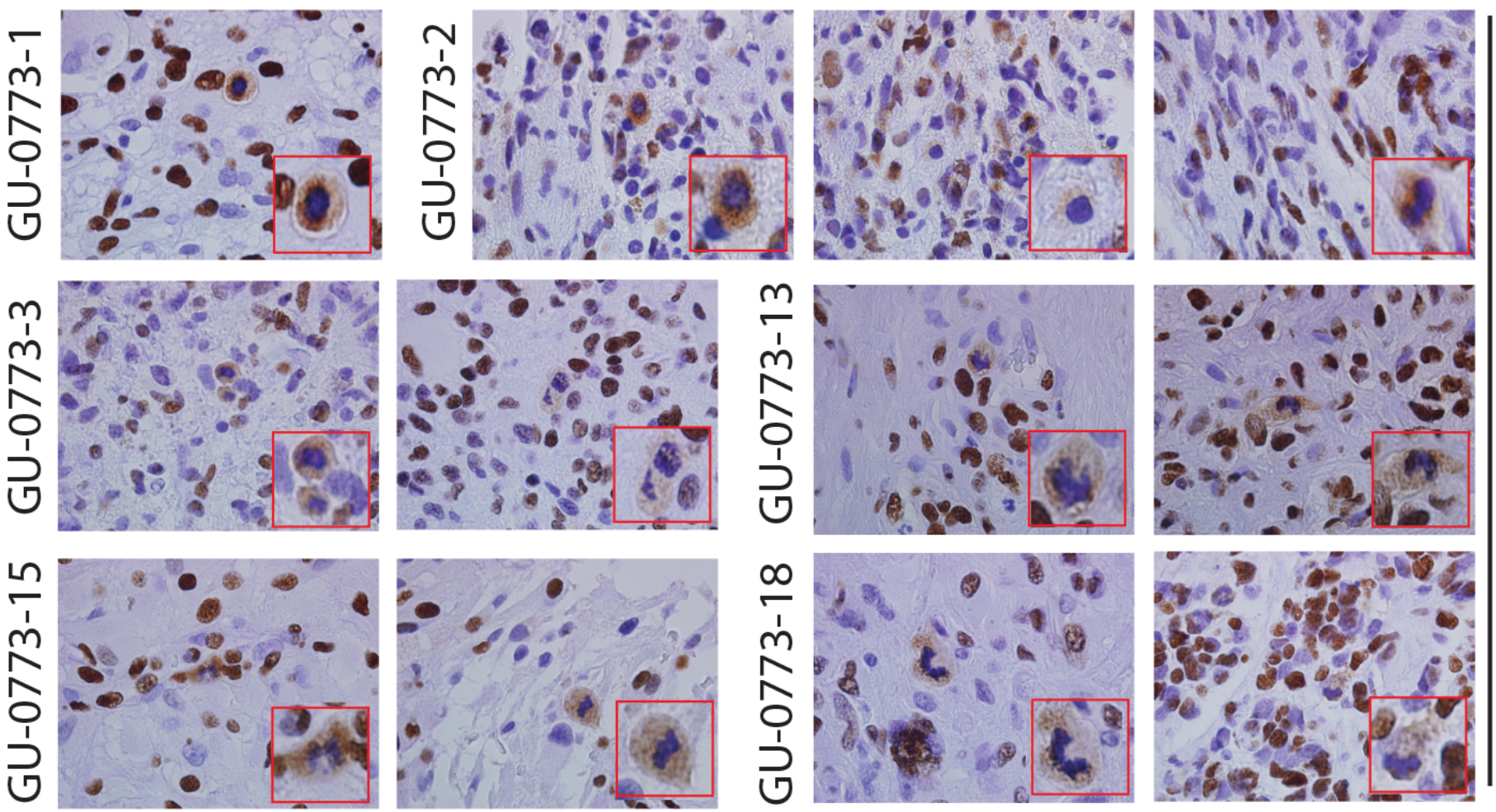
GU-0773-1
GU-0773-2
GU-0773-3
GU-0773-13
GU-0773-15
GU-0773-18
EWSR1